Journal of Materials Research and Technology 36 (2025) 6499–6505

Contents lists available at ScienceDirect

Journal of Materials Research and Technology

journal homepage: www.elsevier.com/locate/jmrt

Retained austenite in multipass high-strength weld metal with a yield strength exceeding 1100 MPa

Daniel Schrittwieser [a,*], Nicole Rinnhofer [a], David Obersteiner [a], Hannes Pahr [b], Oleksandr Glushko [a], Ronald Schnitzer [a]

[a] Department of Materials Science, Montanuniversität Leoben, Franz Josef-Straße 18, 8700 Leoben, Austria
[b] voestalpine Böhler Welding Austria GmbH, Böhler-Welding-Straße 1, 8605 Kapfenberg, Austria

ARTICLE INFO

Handling Editor: P Rios

Keywords:
High-strength weld metal
Weld metal heat-affected zone
Retained austenite
Rietveld refinement
Phase quantification
High-energy X-ray diffraction

ABSTRACT

Retained austenite is an essential phase in various types of steel due to its ability to positively influence mechanical properties. However, in the research field of high-strength weld metals, it is typically considered only as part of martensite-austenite constituents. A detailed quantification of this metastable phase in different heat-affected zone regions and an assessment of its morphology is largely missing. To address this, the present study investigates the distribution and morphology of retained austenite in high-strength multipass all-weld metal with a yield strength exceeding 1100 MPa. A quantitative 2D phase map of retained austenite was generated using high-energy X-ray diffraction and Rietveld refinement. Regardless of the former microstructure, the highest retained austenite contents - up to 7.0 % - are observed in the intercritically reheated zones. These zones replicate the layer structure of the multipass all-weld metal and are surrounded by tempered regions containing less than 2.0 % retained austenite. Using transmission Kikuchi diffraction and electron backscatter diffraction, only minor amounts of stand-alone retained austenite were detected. Consequently, it is expected that the volume fractions of retained austenite may have been underestimated in many former research works about low-alloyed high-strength steels and weld metals.

1. Introduction

Climate change, caused by CO_2 greenhouse gas emissions, was never more topic of debate as in the last years. As one of the largest carbon footprint contributors, particularly the construction industry is challenged to act more environmentally friendly in various process stages [1]. One of the ways to make construction technologies more sustainable and energy efficient is to employ high-strength steels. Due to their superior strength-to-weight ratio, the total construction weight and, correspondingly, materials usage can be significantly reduced [2,3]. The bottleneck of utilizing high-strength steels for construction is the establishment of proper joints. While high-strength steels with yield strength levels up to 1300 MPa are currently available [4], welding consumables have their limitations at 1100 MPa [5]. This is because of difficulties in reaching an acceptable toughness in the weld metal due to the lack of post-processing possibilities and the higher alloying content compared to the high-strength steel base metal [6,7]. Consequently, an advanced microstructure in the weld metal, derived from high-performance consumables combined with precisely coordinated process parameters, forms the foundation for improving high-strength steel joints.

To further advance the development of these high-performance consumables, it is essential to gain a precise understanding of their microstructure and its influences on the mechanical properties under specific process parameters. Therefore, many studies have been published in recent years addressing this subject [7–9]. Since high-strength joints are typically welded using multiple welding passes, especially local microstructural variations play an important role. Reheating of the weld metal by subsequent beads leads to a heat-affected zone (HAZ) within the weld metal, which can be further subdivided into the subcritical (SC), intercritical (IC), fine-grained (FG), and coarse-grained (CG) HAZ, depending on the reheating peak temperature [10–12]. The large number of welding beads can cause parts of these regions to undergo additional reheating. This leads to regions such as the intercritically reheated (IC) CGHAZ, which is recognized as the most critical part of high-strength multipass weld metals regarding toughness [13]. This

* Corresponding author.
E-mail address: daniel.schrittwieser@unileoben.ac.at (D. Schrittwieser).

https://doi.org/10.1016/j.jmrt.2025.04.279
Received 14 March 2025; Received in revised form 10 April 2025; Accepted 26 April 2025
Available online 28 April 2025

inhomogeneous microstructure of multipass weld metals significantly influences the mechanical properties [14] which further leads to a scatter of the Charpy V-notch impact toughness [15–17].

The conventional approach for the microstructural examination of such multipass weld metals is to focus on the most detrimental regions in terms of toughness, such as the CGHAZ and the ICCGHAZ [10,14,15,18]. The low toughness in these regions is typically explained by the coarse microstructure and the presence of martensite-austenite (MA) constituents [15]. These constituents are mixtures of martensite and retained austenite and can have a hardness twice as high as that of the surrounding matrix [18]. Due to their negative impact on the mechanical properties, these zones are the focus of many studies [19,20]. However, stand-alone retained austenite can also appear in high-strength weld metals. Recently, Moon et al. [21] highlighted an improvement in both the tensile strength and impact toughness, achieved through a fine interlocking microstructure that includes film-like retained austenite between the lath boundaries of carbide-free bainite. This morphology of retained austenite is known to be more stable and beneficial for toughness compared to blocky retained austenite [22,23]. Besides the influence on the mechanical properties, retained austenite can additionally act as hydrogen trap and thus reduce the susceptibility of high-strength weld metals to hydrogen-induced cold cracking [24]. The higher the strength of the weld metal, the more martensite is present in the microstructure, which can be accompanied by a higher retained austenite content [9,25]. Therefore, detailed investigations of the total amount, shape, and stability of retained austenite in high-strength weld metals are crucial to further enhance strength levels and to achieve yield strengths exceeding 1300 MPa in the future. Aside from retained austenite in MA constituents, there is a general lack of literature on retained austenite in high-strength weld metals. In particular, the accurate quantification of retained austenite remains a topic of debate due to the influence of the sample preparation and the inconsistency of the results obtained using different methods, such as laboratory X-ray diffraction (XRD) and electron backscatter diffraction (EBSD) [26–28].

To address this long-standing issue, the present study focuses explicitly on retained austenite in a multipass all-weld metal with a yield strength exceeding 1100 MPa established via gas metal arc welding. A 2D distribution of retained austenite was captured using high-energy XRD (HEXRD) and quantified through Rietveld refinement. Over 2000 individual synchrotron measurements were performed in transmission mode, enabling a high spatial resolution and an accurate phase quantification. Additionally, the local amount and morphology of retained austenite were measured using electron microscopy methods such as scanning electron microscopy (SEM), EBSD, and transmission electron microscopy (TEM). The differences in retained austenite content between the HEXRD and the electron microscopy, as well as the influence of the sample preparation on the phase fraction quantification, are critically discussed.

2. Methods

2.1. High-strength all-weld metal

A high-strength multipass all-weld metal was fabricated via gas metal arc welding by utilizing a 1.2 mm metal-cored wire and M21 shielding gas (Ar + 18 % CO_2). To investigate the pure all-weld metal, the 20 mm thick base metals were buffered prior welding and connected with seven layers and three beads per layer in accordance with EN ISO 15792-1 [29]. The corresponding yield strength and Charpy V-notch impact toughness at −40 °C were determined to be 1180 MPa and 40 J. Fig. 1 shows a stereo microscope image of the Nital (3 % HNO_3 with ethanol) etched multipass all-weld metal, containing the upper six layers. The welding parameters and the chemical composition of the high-strength all-weld metal are listed in Tables 1 and 2, respectively.

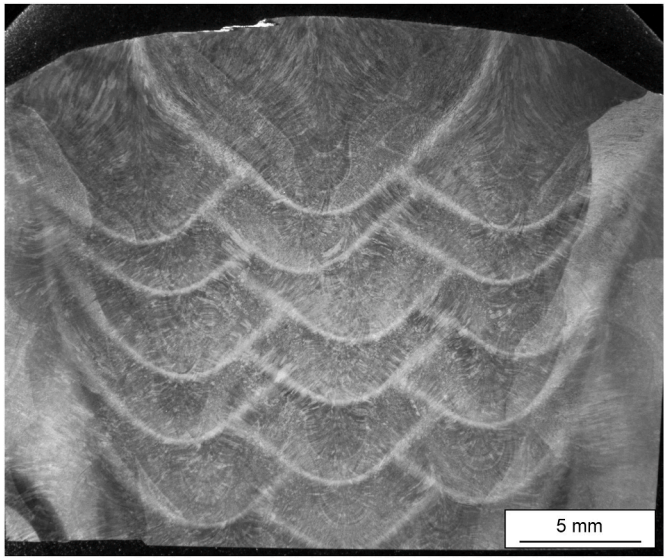

Fig. 1. Stereo microscope image of the multipass high-strength all-weld metal.

Table 1
Welding parameters.

Parameter	Value
Energy input per unit length	7.6 kJ cm^{-1}
$t_{8/5}$ cooling time	4.3 s
Polarity	DC+
Welding position	PA (flat position)
Preheat temperature	100 °C
Interpass temperature	150 °C

Table 2
Chemical composition of the high-strength all-weld metal.

Elements	Fe	C	Si	Mn	Cr	Mo	Ni	V
wt.%	Balance	0.09	0.5	1.5	0.6	0.5	2.9	0.2

2.2. High-energy X-ray diffraction

The HEXRD measurements were conducted at the P07B beamline at the “Deutsches Elektronen Synchrotron” (DESY) in Hamburg, Germany. The sample, a 5 mm thick section extracted from the high-strength all-weld metal, was ground to a grid size of P4000 according to the Federation of European Producers of Abrasives (FEPA) [30]. A monochromatic beam with an average photon energy of 87.1 keV was used to irradiated the sample in transmission mode. A PerkinElmer ERD 1621 flat panel detector with a pixel matrix of 2048 x 2048 and a pixel size of 200 × 200 μm^2 was positioned 1.63 m symmetrically behind the sample to record complete diffraction images. The calibration of the sample-detector distance was carried out using the powder standard LaB_6. A detailed map of the sample, consisting of 2091 images in total, was generated by scanning in x- and y-direction using a beam size of 0.5 × 0.5 mm^2. The experimental setup is illustrated schematically in Fig. 2 (a). Diffraction patterns for the two theta angles in the range between 0° and 7.6° were generated by azimuthal integration using the Python library pyFAI [31].To quantify the phase fraction of austenite based on these diffraction patterns Rietveld refinement was applied using the open source software Profex [32]. This method is based on a comprehensive fit of all peaks occurring in the two theta angular range and is, consequently, less susceptible to texture effects in the weld metal compared to other quantification approaches such as the method of intensity ratio [25,33]. A diffraction pattern including three martensite

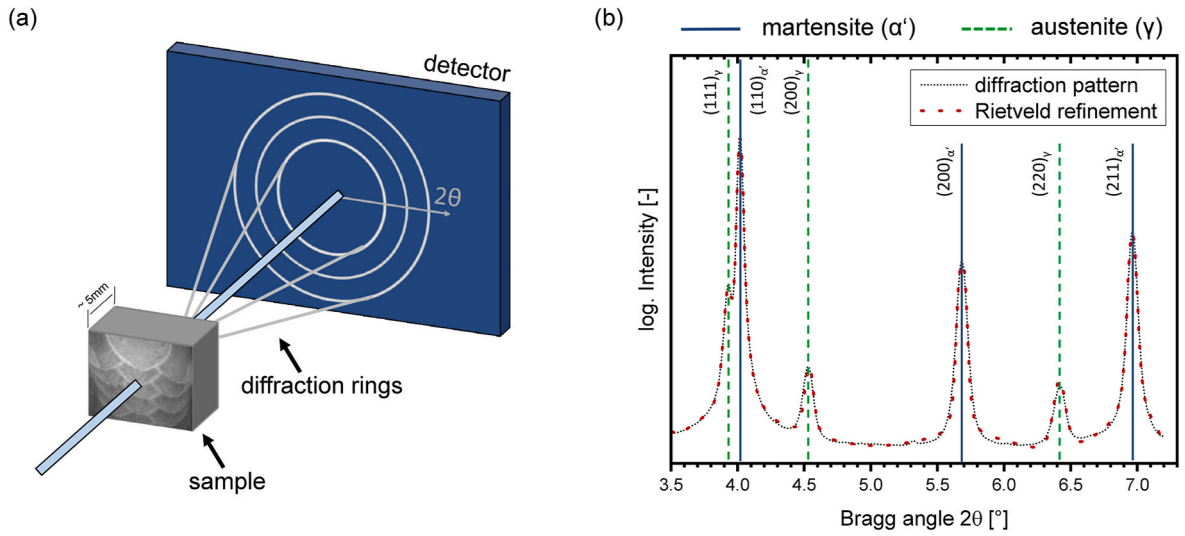

Fig. 2. **(a)** Schematic illustration of the experimental setup. **(b)** Diffraction pattern of a HEXRD measurement including the allocation of the diffraction peaks and the corresponding Rietveld refinement.

(α') and three austenite (γ) peaks within the two theta angle of 3.5° and 7.4°, and the corresponding Rietveld refinement pattern, are illustrated in Fig. 2(b).

2.3. Microstructural characterization

Selected regions of interest were cut from the multipass all-weld metal sample characterized by the synchrotron radiation. These cut outs were then ground and polished, with the final polishing step using 1 μm diamond paste. For the SEM investigation, the metallographic samples were etched with the etchant Nital. EBSD measurements were performed on the same samples with an additional chemical-mechanical polishing step using OPS from Struers. The SEM imaging was conducted on a TESCAN CLARA SEM with an acceleration voltage of 10 kV. For the EBSD measurements an EDAX Hikari EBSD detector implemented in a focused ion beam (FIB) FEI Versa 3D DualBeam was utilized. The applied acceleration voltage was 20 kV and the scanning step size for the low- and high-magnification image 40 nm and 20 nm, respectively. The software EDAX OIM Analysis 8 was used for the data evaluation and a neighbor phase correlation clean-up was applied to all indexed points with a Confidence Index below 0.05.

TEM samples were prepared by FIB lift-out procedure using a FIB FEI Versa 3D DualBeam, with an acceleration voltage of 30 kV and beam currents reduced to 100 pA for the final thinning step. Transmission Kikuchi diffraction (TKD) analysis was carried out in the same microscope with an EDAX Hikari EBSD detector at 30 kV and with a step size of 20 nm. The data was cleaned and analyzed equally to the EBSD measurements. A Thermo Fisher Scientific Talos F200X G2 TEM operating at 200 kV was utilized for bright field scanning-TEM and high-resolution TEM imaging with the corresponding fast Fourier transformation (FFT) investigations. The allocation of the FFT patterns was carried out with the Software CrysTBox [34].

3. Results

3.1. Retained austenite phase distribution

The measured and evaluated quantitative 2D phase distribution map of retained austenite in the multipass all-weld metal is illustrated in Fig. 3. This phase map is stitched together from 2091 single HEXRD measurements with the corresponding Rietveld refinement. As an example, the volume fraction of retained austenite for the diffraction pattern visible in Fig. 2(b) is 7.0 %. This diffraction pattern was recorded

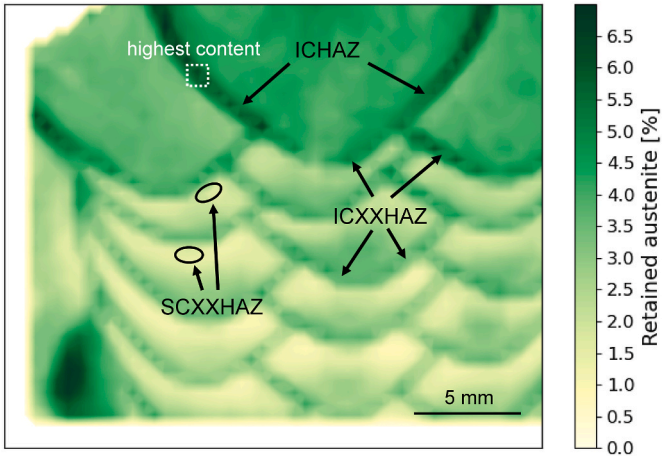

Fig. 3. Quantitative retained austenite phase map calculated with Rietveld refinement. The highest phase fractions are found in the intercritically reheated zones, independent of the former microstructure. These zones replicate the morphology of the welding beads.

in the ICHAZ, marked by the white rectangle in Fig. 3. In this single reheated zone, the highest levels of retained austenite of the entire multipass all-weld metal are detected. However, when the already deposited weld metal of former welding beads gets intercritically reheated, there is still an increased amount of retained austenite (3.0 %–5.5 %) compared to the surrounding matrix. This is evident in the darker regions according to the color scale in Fig. 3. The formation of these intercritically reheated zones with enhanced content of retained austenite is independent of whether the former microstructure belonged to a SCHAZ, ICHAZ, FGHAZ, or CGHAZ. Therefore, these regions are referred to as ICXXHAZ in Fig. 3, with the "XX" representing the unknown type of former microstructure. Comparing the retained austenite phase map with the Nital etched metallographic overview in Fig. 1, these ICXXHAZ can be recognized as bright areas replicating the morphology of the welding beads. The lowest content of retained austenite (<2.0 %) is visible in the subcritical reheated zones (marked as SCXXHAZ), located directly beneath the ICXXHAZ. An overall decrease in the content of retained austenite occurs from the top of the multipass all-weld metal to the bottom. The high phase fraction of retained austenite in the lower-left corner in Fig. 3 can be neglected, as this

region is located in the buffer layer of the joint.

3.2. Morphology of retained austenite

Next to the quantification, the morphology of retained austenite was examined. The ICHAZ, highlighted in Fig. 3, was selected as the region of interest due to its high retained austenite phase content. A comparison of this zone to the as-deposited weld metal in the last bead is depicted in Fig. 4. Fig. 4(a) illustrates the chaotic martensitic microstructure of the last bead. The ICHAZ in Fig. 4(b) is divided into a tempered region, which did not undergo austenitization during intercritical heating, and an intercritically austenitized region, which is referred to as the re-austenitized region in the present work. The tempered region is characterized by a flat appearance and more heavily etched grains. The re-austenitized region shows a similar microstructure as the as-deposited weld metal in the last bead. During the brief reheating, this re-austenitized region transforms into austenite and enriches in C due to the higher solubility. As a result, after cooling, C-enriched martensite is formed, and therefore, the highest retained austenite content is expected in this region of the ICHAZ [25].

The EBSD images in Fig. 5 show inverse pole Figure (IPF) and phase maps of the ICHAZ. The IPF maps display the crystallographic orientations parallel to the welding direction, as shown in the insets in Fig. 5(a) and (c). In the phase maps, the face-centered cubic (fcc) grains are referred to as retained austenite. Due to the low C-content in the current all-weld metal and the pronounced tempering condition in the ICHAZ, the c/a ration of the body-centered tetragonal structure of martensite is close to one [35]. Consequently, the body-centered cubic (bcc) grains show the martensitic phase. In the lower region of Fig. 5(a), some microstructurally small islands appear, which are likely associated with MA constituents. However, no retained austenite is observed by applying a scanning step size of 40 nm, neither within these islands nor in the surrounding microstructure, as illustrated in the phase map in Fig. 5(b). Higher resolution images of the ICHAZ with a scanning step size of 20 nm in Fig. 5(c) and (d) enabled the detection of retained austenite. The three major retained austenite islands, which are colored red in the phase map in Fig. 5(d), share the same crystallographic orientation as evident from Fig. 5(c). These islands appear as stand-alone phases and are not parts of MA constituents. The area fraction of retained austenite at this location is 0.50 % according to the EBSD data, as seen in Fig. 5(d).

Fig. 6 shows a TEM lamella prepared from the re-austenitized region of the ICHAZ, where the highest amount of retained austenite is expected. The TKD-IPF map in Fig. 6(a) reveals the fine-grained structure of this region, while the TKD-phase map in Fig. 6(b) shows a volume fraction of 0.10 % retained austenite. The retained austenite appears as stand-alone phase and not as a part of MA constituents. Moreover, these stand-alone phases again share the same crystallographic orientation. To confirm the results of the TKD-phase map, high-resolution TEM with a corresponding FFT was applied to an austenitic island. As shown in Fig. 6(c), the grain identified as fcc in the TKD-phase map was also identified as austenite through the FFT analysis.

4. Discussion

4.1. Influence of the quantification methods and sample preparation on retained austenite

The most commonly used methods for measuring the amount of retained austenite are XRD and EBSD. Both methods primarily detect signals from the near-surface region of the metallographic sample. For example, in the study of Pinto et al. [27], the penetration depths of EBSD and XRD were estimated to be approximately 150 nm and 7.5 μm, respectively. Although XRD penetrates deeper into the material than EBSD, it still analyses only the near-surface region, making proper sample preparation a crucial step [27]. Consequently, many studies have addressed the influence of the sample preparation on the volume fraction of retained austenite. The challenge in detecting this metastable phase near the surface is its tendency to transform into martensite under mechanical strain [28]. Therefore, the goal of a suitable sample preparation is to achieve a strain-free surface that preserves the retained austenite content at its original level. Chemical-mechanical polishing, electropolishing, and ion sputtering are common methods for the preparation. However, the most appropriate sample preparation depends on both the investigated material and the used investigation method [26–28,36].

In the current study, the usage of HEXRD in transmission eliminates any potential surface preparation effects, however, EBSD is still required to observe the morphology of retained austenite. Pre-investigations considering the sample preparation showed that chemical-mechanical polishing with OPS from Struers leads to the highest quality Kikuchi patterns for the all-weld metal used in this study. Electropolishing resulted in a large amount of shadows due to surface relief and ion milling in a lack of retained austenite, regardless of the process parameters selected. However, although the sample preparation was optimized for the current all-weld metal, Fig. 5 illustrates that retained austenite was detected only to a small extent compared to the HEXRD measurements in Fig. 3. Each measurement point of this map represents averaged information from a sample volume of about 0.5 x 0.5 × 5 mm^3, making the results independent of the surface condition of the sample. Consequently, the results of this advanced method serve as a reference for the actual amount of retained austenite in the microstructure. Only

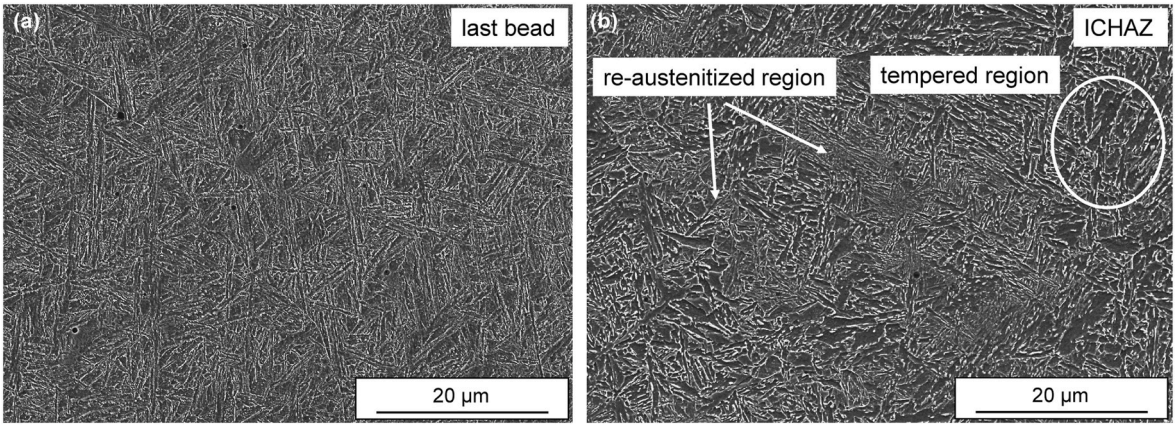

Fig. 4. SEM image of the **(a)** last bead and the **(b)** ICHAZ. The last bead contains a chaotic martensitic microstructure. In the ICHAZ, the microstructure is divided into a tempered and a re-austenitized region.

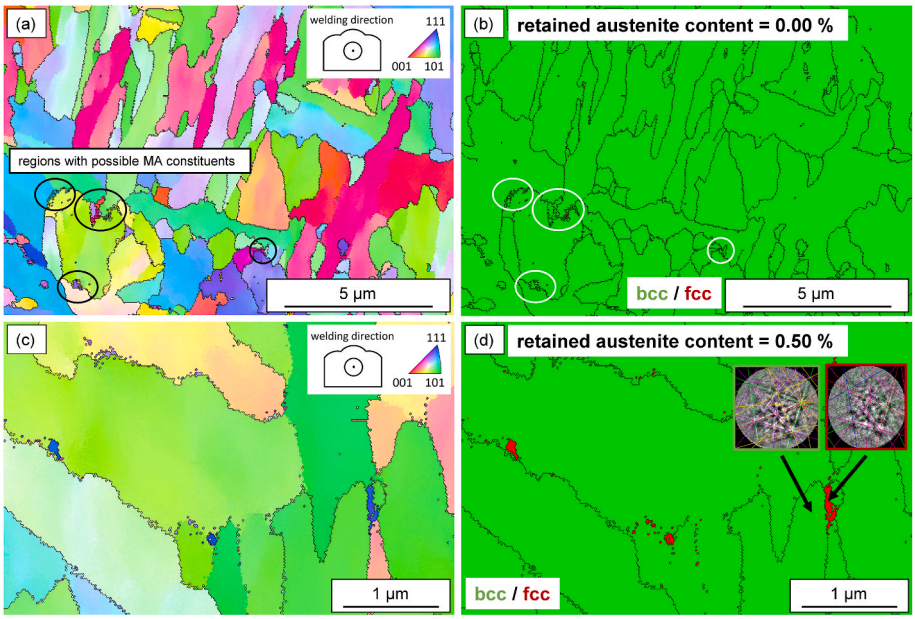

Fig. 5. **(a)** IPF and **(b)** phase map of the ICHAZ with low magnification and a step size of 40 nm. **(c)** IPF and **(d)** phase map of the ICHAZ with high magnification and a step size of 20 nm with the insets showing the Kikuchi patterns of a bcc and fcc phase. The IPF maps display the crystallographic orientations parallel to the welding direction. No fcc phase, i.e. retained austenite, was detected at low magnification, but 0.50 % at high magnification.

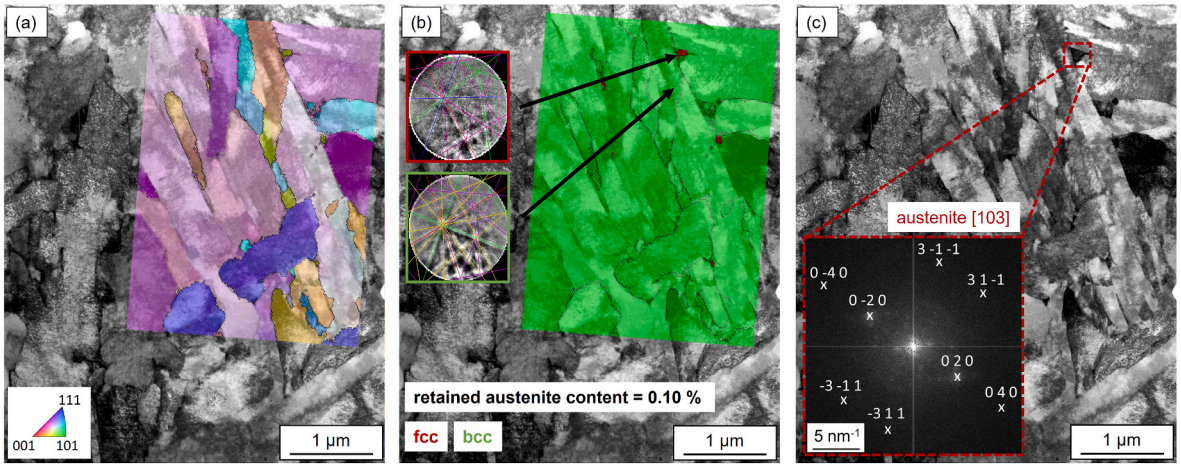

Fig. 6. TEM bright field image of the re-austenitized region in the ICHAZ. **(a)** Overlaid with the TKD-IPF map, showing the crystallographic orientations. **(b)** Overlaid with the TKD-phase map including two Kikuchi patterns representing the fcc and bcc phase. **(c)** Includes the FFT-pattern of an austenitic phase.

small retained austenite phase regions, on the order of a few tens of nanometers, are difficult to detect via HEXRD due to peak broadening [37,38]. However, the high retained austenite values measured in this work can be considered realistic, or even conservative, since undetectable nanoscale regions would imply that the actual retained austenite content in the weld metal HAZ is even slightly higher than measured.

The high-magnification EBSD phase map in Fig. 5(d) only shows 0.50 % of retained austenite, compared to 5.5 %–7.0 % in the HEXRD map in Fig. 3. Consequently, even the most suitable preparation method for the used material leads to a significant transformation of retained austenite. Additionally, the detection limit of EBSD may contribute to the underestimation of the amount of retained austenite. Therefore, TKD was applied to a TEM lamella to achieve higher resolution. However, even with the TKD-phase map, only 0.10 % retained austenite was detected, as shown in Fig. 6(b). According to Tolchard et al. [28], removing 15–20 µm material from the surface is necessary to reach a region free from mechanical deformation caused by previous sample preparation and to reveal the full amount of retained austenite. Consequently, the TEM lamella was still taken from this deformed surface region. Thus, without the ability to electrolytically remove 15–20 µm from the surface, it is nearly impossible to fully reveal the retained austenite using electron microscopy methods. Another problem is that the preparation of the TEM lamella with a FIB can lead to a reduction in retained austenite due to the enrichment of Ga^{+}, which acts as ferrite stabilizer [39–42]. This phenomenon may explain the lower retained austenite content compared to EBSD. However, the locally limited observation area and the corresponding lack of statistics are considered as the main contribution factors for that. Furthermore, since retained austenite is less constrained at the surface compared to the bulk, it may undergo further transformation to martensite [43]. Another interesting fact is that the EBSD- and TKD-phase maps reveal only stand-alone retained austenite. However, in weld metals, the majority of retained austenite is commonly expected to be located in MA constituents within the reheated zones. Due to limitations in resolution, only coarse MA constituents can be resolved with EBSD and it is challenging to find retained austenite in these constituents, as visible in Fig. 5(a) and (b)

[18]. Therefore, high-resolution TEM would be necessary to identify retained austenite in MA constituents, but a drawback of this method is the lack of statistics.

Summarized, EBSD and TKD are suitable methods to reveal the morphology of retained austenite, but it is hardly possible to reliably quantify the amount of this metastable phase. This is particularly true for low-alloyed steel microstructures with minor amounts of unstable retained austenite, such as the all-weld metal investigated in this study. The reasons include strain-induced transformation of retained austenite, reduced constraint at the surface, and limitations in resolution. Consequently, the authors propose that HEXRD is the most suitable method for quantifying retained austenite due to its high brilliance and beam quality, independence of the sample preparation artefacts and high spatial resolution. Additionally, the high absolute values of retained austenite observed in this study suggest that the volume fractions of retained austenite may have been underestimated in many former research works about low-alloyed high-strength steels and weld metals since several years.

4.2. Distribution of retained austenite

As visible in Fig. 3, the highest austenite contents are found in the ICHAZ and ICXXHAZ, which closely replicate the layer structure of the multipass all-weld metal. This observation underlines that the diffusion of C to austenite during the intercritically reheating step is the key driving force for the stabilization of retained austenite in high-strength multipass weld metal. Directly underneath the ICXXHAZ, in the SCXXHAZ, the lowest austenite contents are recognized due to the pronounced tempering effect at peak temperatures just below the ferrite/austenite two phase region. Furthermore, Fig. 3 reveals an overall decrease in retained austenite from the top to the bottom. This trend can be attributed to the elevated heat treatment cycles and the corresponding tempering of retained austenite in the lower regions, resulting from the increased number of subsequent beads. Despite this general decrease, regions with elevated retained austenite content are dispersed over the whole multipass all-weld metal.

4.3. Influence on mechanical properties

Retained austenite is known to significantly influence the strength and toughness of steel microstructures, with filmy retained austenite being the most beneficial morphology for enhancing this properties [21,23,44]. According to Wang et al. [45], already 2.5 % of stable retained austenite is sufficient to improve the toughness, which is lower than the values observed in the ICHAZ and ICXXHAZ in this study. Additionally, retained austenite has the ability to trap hydrogen, which can reduce the susceptibility of weld metal to hydrogen-induced cold cracking [46]. Park et al. [24] confirmed this H-trapping effect in high-strength weld metal containing 4 % retained austenite. Zenitani et al. [47] even developed a low-transformation-temperature welding consumable with retained austenite in order to explicitly prevent cold cracking. Consequently, the retained austenite in the present all-weld metal likely contributes to increase the toughness while also acting as a hydrogen trap. However, to which extend this metastable phase contributes to improved properties remains uncertain. As strength levels increase to meet future demands, higher retained austenite contents are expected in multipass weld metals. Therefore, retained austenite is a crucial phase in the further development of high-strength weld metals.

5. Conclusions

In the present study, a quantitative 2D phase map of retained austenite was established for a high-strength multipass all-weld metal using HEXRD and Rietveld refinement. The morphology of retained austenite was analyzed with SEM, EBSD, TKD and TEM, leading to the following conclusions.

- The highest retained austenite contents of the investigated multipass all-weld metal (up to 7.0 %) are observed in the ICHAZ.
- Elevated retained austenite contents are present in all intercritically reheated zones, regardless of the initial microstructure or weld bead position.
- The lowest retained austenite contents (below 2.0 %) are observed directly beneath the intercritically reheated zones, resulting from exposure to the highest possible tempering temperature without undergoing austenitic transformation.
- The retained austenite phase map replicates the layer structure of the multipass all-weld metal.
- The overall content of retained austenite decreases from the top to the bottom of the all-weld metal.
- Retained austenite quantification using EBSD and TKD considerably underestimates the actual values.
- With these methods, retained austenite was only detected as a stand-alone phase and not within MA constituents.

Due to potentially positive effects on the toughness and the hydrogen trapping ability, small amounts of retained austenite with an adequate thin-film morphology might be required for future high-strength weld metal design.

CRediT authorship contribution statement

Daniel Schrittwieser: Conceptualization, Methodology, Investigation, Writing – original draft, Visualization, Project administration. **Nicole Rinnhofer:** Investigation, Writing – review & editing. **David Obersteiner:** Investigation, Writing – review & editing. **Hannes Pahr:** Resources, Writing – review & editing. **Oleksandr Glushko:** Writing – review & editing. **Ronald Schnitzer:** Resources, Supervision, Writing – review & editing.

Data availability

Data will be made available on request.

Declaration of generative AI and AI-assisted technologies in the writing process

During the preparation of this work the authors used ChatGPT in order to improve the readability and language. After using this tool, the authors reviewed and edited the content as needed and take full responsibility for the content of the publication.

Funding

No funding was obtained for this study.

Declaration of competing interest

The authors declare that they have no known competing financial interests or personal relationships that could have appeared to influence the work reported in this paper.

Acknowledgment

We acknowledge DESY (Hamburg, Germany), a member of the Helmholtz Association HGF, for the provision of experimental facilities. Parts of this research were carried out at PETRA III. Beamtime was allocated for proposal H-20010018. Financial support from the Austrian Research Promotion Agency (FFG) in the project 3DnanoAnalytics (Grant No. FFG-No. 858040) is also gratefully acknowledged. Furthermore, the authors would like to thank Sebastian Leodolter from voestalpine Böhler Welding Austria GmbH for his valuable support.

References

[1] Sizirici B, Fseha Y, Cho CS, Yildiz I, Byon YJ. A review of carbon footprint reduction in construction industry, from design to operation. Materials 2021;14 (20):6094. https://doi.org/10.3390/ma14206094.

[2] Saufnay L, Demonceau J. Economic and environmental assessment of high-strength steel grades. ce/papers 2023;6(3–4):527–32. https://doi.org/10.1002/cepa.2291.

[3] Ban H, Shi G. A review of research on high-strength steel structures. Proc Inst Civ Eng Struct Build 2018;171(8):625–41. https://doi.org/10.1680/jstbu.16.00197.

[4] Tümer M, Schneider-Bröskamp C, Enzinger N. Fusion welding of ultra-high strength structural steels – a review. J Manuf Process 2022;82(May):203–29. https://doi.org/10.1016/j.jmapro.2022.07.049.

[5] Haslberger P, Holly S, Ernst W, Schnitzer R. Microstructure and mechanical properties of high-strength steel welding consumables with a minimum yield strength of 1100 MPa. J Mater Sci 2018;53(9):6968–79. https://doi.org/10.1007/s10853-018-2042-9.

[6] Rauch R, Kapl S, Posch G, Radlmayr K. High strength low alloy steel weldments with accommodated qualities to the base metal. BHM Berg- Hüttenmännische Monatsh 2012;157(3):102–7. https://doi.org/10.1007/s00501-012-0060-5.

[7] Schrittwieser D, Pahr H, Musi M, Landefeld A, Glushko O, Schnitzer R. Revealing the embrittlement phenomena after post-weld heat treatment of high-strength weld metal using high-resolution microscopy. J Mater Res Technol 2024;33:5289–98. https://doi.org/10.1016/j.jmrt.2024.10.186.

[8] Keehan E, Zachrisson J, Karlsson L. Influence of cooling rate on microstructure and properties of high strength steel weld metal. Sci Technol Weld Join 2010;15(3): 233–8. https://doi.org/10.1179/136217110X12665048207692.

[9] Jorge JCF, Souza LFGD, Mendes MC, Bott IS, Araújo LS, Santos VRD, et al. Microstructure characterization and its relationship with impact toughness of C-Mn and high strength low alloy steel weld metals - a review. J Mater Res Technol 2021; 10:471–501. https://doi.org/10.1016/j.jmrt.2020.12.006.

[10] Wang XL, Wang XM, Shang CJ, Misra RDK. Characterization of the multi-pass weld metal and the impact of retained austenite obtained through intercritical heat treatment on low temperature toughness. Mater Sci Eng A 2016;649:282–92. https://doi.org/10.1016/j.msea.2015.09.030.

[11] Spanos G, Fonda RW, Vandermeer RA, Matuszeski A. Microstructural changes in HSLA-100 steel thermally cycled to simulate the heat-affected zone during welding. Metall Mater Trans A 1995;26(12):3277–93. https://doi.org/10.1007/BF02669455.

[12] Falkenreck T, Kromm A, Böllinghaus T. Investigation of physically simulated weld HAZ and CCT diagram of HSLA armour steel. Weld World 2018;62(1):47–54. https://doi.org/10.1007/s40194-017-0511-4.

[13] You Y, Shang C, Chen L, Subramanian S. Investigation on the crystallography of the transformation products of reverted austenite in intercritically reheated coarse grained heat affected zone. Mater Des 2013;43:485–91. https://doi.org/10.1016/j.matdes.2012.07.015.

[14] Kang Y, Park G, Jeong S, Lee C. Correlation between microstructure and low-temperature impact toughness of simulated reheated zones in the multi-pass weld metal of high-strength steel. Metall Mater Trans A. 2018;49(1):177–86. https://doi.org/10.1007/s11661-017-4384-3.

[15] Quintana MA, Babu SS, Major J, Dallam C, James M. Weld metal toughness: sources of variation. International Pipeline Conference; 2010. p. 599–608.

[16] Cao R, Yuan JJ, Xiao ZG, Ma JY, Mao GJ, Zhang XB, et al. Sources of variability and lower values in toughness measurements of weld metals. J Mater Eng Perform 2017;26(6):2472–83. https://doi.org/10.1007/s11665-017-2686-7.

[17] Song HY, Evans GM, Babu SS. Effect of microstructural heterogeneities on scatter of toughness in multi-pass weld metal of C-Mn steels. Sci Technol Weld Join 2014; 19(5):376–84. https://doi.org/10.1179/1362171814Y.0000000194.

[18] Schrittwieser D, Marin Morales D, Pahr H, Lumper LA, Glushko O, Schnitzer R. Microstructural insights into the coarse-grained heat-affected zone of a high-strength all-weld metal: Development of a continuous cooling transformation diagram. Weld World 2025;69(3):813–23. https://doi.org/10.1007/s40194-024-01904-4.

[19] Li X, Ma X, Subramanian SV, Shang C, Misra RDK. Influence of prior austenite grain size on martensite–austenite constituent and toughness in the heat affected zone of 700MPa high strength linepipe steel. Mater Sci Eng A 2014;616:141–7. https://doi.org/10.1016/j.msea.2014.07.100.

[20] Luo X, Chen X, Wang T, Pan S, Wang Z. Effect of morphologies of martensite–austenite constituents on impact toughness in intercritically reheated coarse-grained heat-affected zone of HSLA steel. Mater Sci Eng A 2018;710:192–9. https://doi.org/10.1016/j.msea.2017.10.079.

[21] Moon J, Bae G, Jeong BY, Shin C, Kwon MJ, Kim DI, et al. Ultrastrong and ductile steel welds achieved by fine interlocking microstructures with film-like retained austenite. Nat Commun 2024;15(1):1301. https://doi.org/10.1038/s41467-024-45470-1.

[22] Bhadeshia HKDH, Edmonds DV. Bainite in silicon steels: new composition–property approach Part 1. Met Sci. 1983;17(9):411–9. https://doi.org/10.1179/030634583790420646.

[23] Ding R, Tang D, Zhao A. A novel design to enhance the amount of retained austenite and mechanical properties in low-alloyed steel. Scr Mater 2014;88:21–4. https://doi.org/10.1016/j.scriptamat.2014.06.014.

[24] Park YD, Maroef IS, Landau A, Olson DL. Retained Austenite as a hydrogen trap in steel welds. Weld J 2002;81(2).

[25] Jatczak CF. Retained austenite and its measurement by X-ray diffraction. In: SAE technical papers; 1980. p. 1657–76. https://doi.org/10.4271/800426.

[26] Elstad KR, Andresen BS, Karlsen M, Westermann I, Hjelen J. The effect of sample preparation on quantification of retained austenite in supermartensitic stainless steel studied by EBSD and XRD. Proc Int Offshore Polar Eng Conf 2016:454–8.

[27] Pinto LA, Pérez Escobar D, Santos OSH, Lopes NIA, Carneiro JRG, Ribeiro-Andrade R. Influence of surface preparation method on retained austenite quantification. Mater Today Commun 2020;24:101226. https://doi.org/10.1016/j.mtcomm.2020.101226.

[28] Tolchard JR, Sømme A, Solberg JK, Solheim KG. On the measurement of austenite in supermartensitic stainless steel by X-ray diffraction. Mater Charact 2015;99: 238–42. https://doi.org/10.1016/j.matchar.2014.12.005.

[29] Austrian Standards International. Schweißzusätze - Prüfverfahren, ÖNORM EN ISO 15792-1:2020. 2020.

[30] Federation of European Producers of Abrasives. FEPA standard 43-2:2017: grains of fused aluminium oxide, silicon carbide, and other abrasive materials for coated abrasives—microgrits P240 to P5000. 2017.

[31] Kieffer J, Valls V, Blanc N, Hennig C. New tools for calibrating diffraction setups. J Synchrotron Radiat 2020;27(2):558–66. https://doi.org/10.1107/S1600577520000776.

[32] Doebelin N, Kleeberg R. Profex : a graphical user interface for the Rietveld refinement program BGMN. J Appl Crystallogr 2015;48(5):1573–80. https://doi.org/10.1107/S1600576715014685.

[33] Epp J. X-ray diffraction (XRD) techniques for materials characterization. In: Materials characterization using nondestructive evaluation (NDE) methods. Elsevier; 2016. p. 81–124. https://doi.org/10.1016/B978-0-08-100040-3.00004-3.

[34] Klinger M. More features, more tools, more CrysTBox. J Appl Crystallogr 2017;50: 1226–34. https://doi.org/10.1107/S1600576717006793.

[35] Lu Y, Yu H, Sisson RD. The effect of carbon content on the c/a ratio of as-quenched martensite in Fe-C alloys. Mater Sci Eng A 2017;700:592–7. https://doi.org/10.1016/j.msea.2017.05.094.

[36] Koll L, Tsipouridis P, Werner EA. Preparation of metallic samples for electron backscatter diffraction and its influence on measured misorientation. J Microsc 2011;243(2):206–19. https://doi.org/10.1111/j.1365-2818.2011.03495.x.

[37] Schwaighofer E, Staron P, Rashkova B, Stark A, Schell N, Clemens H, et al. In situ small-angle X-ray scattering study of the perovskite-type carbide precipitation behavior in a carbon-containing intermetallic TiAl alloy using synchrotron radiation. Acta Mater 2014;77:360–9. https://doi.org/10.1016/j.actamat.2014.06.017.

[38] Erdely P, Staron P, Stark A, Klein T, Clemens H, Mayer S. In situ and atomic-scale investigations of the early stages of γ precipitate growth in a supersaturated intermetallic Ti-44Al-7Mo (at.%) solid solution. Acta Mater 2019;164:110–21. https://doi.org/10.1016/j.actamat.2018.10.042.

[39] Bała P, Gajewska M, Cios G, Kawałko J, Wątroba M, Bednarczyk W, et al. Effect of GA+ ion beam on the stability of retained austenite in high carbon steel. Mater Charact 2022;186:111766. https://doi.org/10.1016/j.matchar.2022.111766.

[40] Basa A, Thaulow C, Barnoush A. Chemically induced phase transformation in Austenite by focused ion beam. Metall Mater Trans A. 2014;45(3):1189–98. https://doi.org/10.1007/s11661-013-2101-4.

[41] Babu RP, Irukuvarghula S, Harte A, Preuss M. Nature of gallium focused ion beam induced phase transformation in 316L austenitic stainless steel. Acta Mater 2016; 120:391–402. https://doi.org/10.1016/j.actamat.2016.08.008.

[42] Knipling KE, Rowenhorst DJ, Fonda RW, Spanos G. Effects of focused ion beam milling on austenite stability in ferrous alloys. Mater Charact 2010;61(1):1–6. https://doi.org/10.1016/j.matchar.2009.09.013.

[43] Bojack A, Zhao L, Morris PF, Sietsma J. In-situ determination of austenite and martensite formation in 13Cr6Ni2Mo supermartensitic stainless steel. Mater Charact 2012;71:77–86. https://doi.org/10.1016/j.matchar.2012.06.004.

[44] Xie ZJ, Yuan SF, Zhou WH, Yang JR, Guo H, Shang CJ. Stabilization of retained austenite by the two-step intercritical heat treatment and its effect on the toughness of a low alloyed steel. Mater Des 2014;59:193–8. https://doi.org/10.1016/j.matdes.2014.02.035.

[45] Wang C, Li C, Dai L, Yang X, Han J, Cui S, et al. Simultaneously enhancing strength and fracture toughness via tailoring the microstructure in X80 girth weld metal. J Mater Res Technol 2024;29:3096–107. https://doi.org/10.1016/j.jmrt.2024.01.283.

[46] Kasuya T, Hashoba Y, Inoue H, Nakamura S, Takai K. Hydrogen diffusion in weld metals with retained austenite and its application to the welded joints. Weld World 2013;57(4):581–93. https://doi.org/10.1007/s40194-013-0056-0.

[47] Zenitani S, Hayakawa N, Yamamoto J, Hiraoka K, Morikage Y, Kubo T, et al. Development of new low transformation temperature welding consumable to prevent cold cracking in high strength steel welds. Sci Technol Weld Join 2007;12 (6):516–22. https://doi.org/10.1179/174329307X213675.